THE JOURNAL OF PHYSICAL CHEMISTRY C

Article

pubs.acs.org/JPCC

Nanocrystalline and Polyicosahedral Structure of a Nanospike Generated on Metal Surface Irradiated by a Single Femtosecond Laser Pulse

Chengping Wu and Leonid V. Zhigilei*

Department of Materials Science and Engineering, University of Virginia, 395 McCormick Road, Charlottesville, Virginia 22904-4745, United States

ABSTRACT: Short pulse laser irradiation of metal targets can trigger a cascade of highly nonequilibrium processes leading to the formation of unique surface structures of interest to various practical applications. In this paper, we report the results of a large-scale atomistic simulation predicting the generation of a ~200 nm long frozen nanospike on the surface of a Ag target irradiated by a femtosecond laser pulse. The simulation provides detailed information on the mechanisms responsible for the formation of the nanospike and the processes that define its complex nanostructure. The competing contributions of the epitaxial regrowth of the solid part of the target and the homogeneous nucleation of new crystallites triggered by the strong undercooling of the liquid regions are found to produce a remarkable variability of the structural motifs coexisting in different regions of the frozen nanospike. The homogeneous solidification, in particular, proceeds along two distinct paths selected at the nucleation stage and produces markedly different nanostructures in different parts of the nanospike, namely, nanograins with mixed fcc/hcp structure and a continuous network of pentagonal twinned structural elements arranged into a polyicosahedral structure.

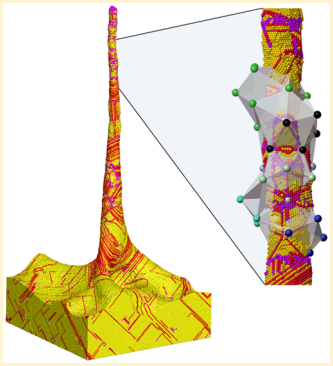

1. INTRODUCTION

Short pulse laser processing of metal surfaces typically involves fast melting of a thin surface layer of the irradiated target followed by rapid cooling due to the heat conduction to the bulk of the target and resolidification. The high thermal conductivity of metals combined with the strong localization of the laser energy deposition can result in very high cooling rates of up to 10^{12} K/s[1−4] and can bring the melted surface layer to a state of strong undercooling below the equilibrium melting temperature. The process of rapid solidification proceeding under conditions of deep undercooling can involve a range of competing processes, including epitaxial regrowth of the substrate, nucleation of crystallites throughout the undercooled melted region, and material reheating due to the release of the latent heat of solidification. At laser fluences that are close to or above the spallation threshold, the solidification proceeds simultaneously with photomechanical generation of subsurface voids that may evolve into a foamy structure of interconnected liquid bridges connecting the spalled layer with the bulk of the target.[5] The eventual breakup and solidification of the liquid bridges can contribute to the formation of complex multiscale surface morphology commonly observed on metal surfaces irradiated by short laser pulses.[6−9]

The experimental pump−probe studies provide valuable data on the kinetics (characteristic time scales) of the laser-induced melting and resolidification[3,10−12] but yield almost no information on the evolution of the microstructure in the irradiated targets. Moreover, the time-resolved probing of the solidification process occurring in the spallation regime is virtually impossible as the "view" of the surface is obscured by the spalled liquid layer/droplets that remain in a close proximity of the target during the time of the solidification.

Because of the difficulties of the direct experimental probing of the rapid laser-induced structural transformations, the atomistic modeling[4,13−16] is playing an increasingly important role in providing reliable physical interpretation of the results of *ex situ* characterization of the microstructural changes produced by short-pulse laser irradiation.[9,17−20] In particular, the results of a recent large-scale atomistic simulation of femtosecond laser irradiation of a single-crystal Ag target[15] have suggested an explanation for experimental observations of "surface swelling" and subsurface voids generated at laser fluences just below the spallation threshold.[15,21−23] The simulation also predicts the formation of a nanocrystalline surface layer of the target featuring random crystallographic orientation of nanograins and a high density of stacking faults, twins, and nanoscale twinned structural elements with 5-fold symmetry.

In this paper we report an extension of these calculations to the spallation regime, where the cooling, advancement of the solidification front, and nanocrystallization of the surface region occur concurrently with the hydrodynamic flow, coarsening, and breakdown of the liquid bridges. The broad range of the undercooling conditions realized in the course of the surface solidification and the small dimensions of the nanoscale surface features set the stage for the competition between different solidification mechanisms leading to the remarkable variability

Received: January 1, 2016
Revised: February 6, 2016
Published: February 8, 2016

DOI: 10.1021/acs.jpcc.6b00013
J. Phys. Chem. C 2016, 120, 4438−4447

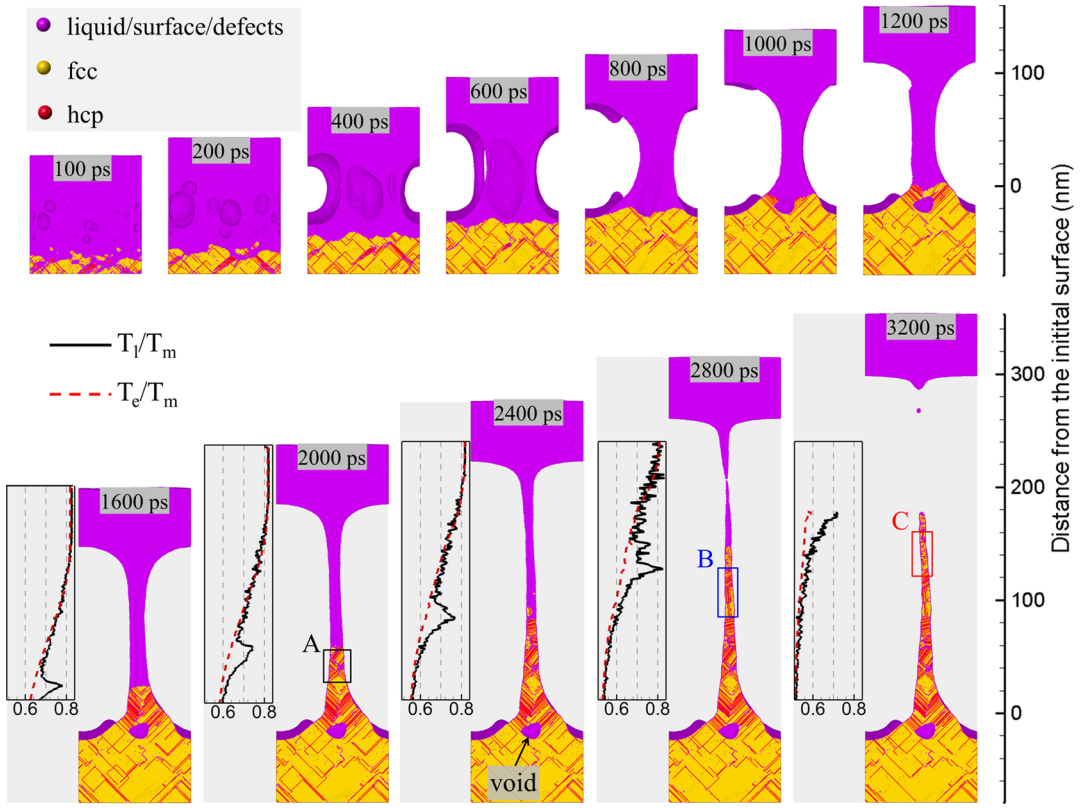

Figure 1. Snapshots of atomic configurations predicted in a TTM-MD simulation of laser spallation of a bulk Ag target irradiated by a 100 fs laser pulse at an absorbed fluence of 900 J/m^2. The laser irradiation is directed from the top of the figure. To provide a clear view of the resolidification process, the atomic configurations are cross-sectioned by a plane passing through the liquid bridge/frozen nanospike generated in the spallation process. The views of the cross sections are shown along the [010] direction. The atoms are colored according to their local structural environment,[14,33] so that the fcc and hcp atoms are yellow and red, respectively, while the atoms that belong to the melted parts of the target, crystal defects (point defects, dislocations, or grain boundaries), or free surfaces are purple. The black, blue, and red rectangles marked as A, B, and C, outline the regions for which snapshots are shown in Figures 4, 5, and 6, respectively. The insets in the bottom row show the temperature profiles in the corresponding parts of the system, from 10 to 240 nm above the initial surface. The solid black lines and the dashed red lines show the lattice and electron temperatures, respectively.

of the structural elements present within the frozen surface features.

2. COMPUTATIONAL MODEL

The large-scale atomistic simulation of the laser-induced melting, spallation, and resolidification of a bulk single crystal Ag (001) target is performed with a hybrid atomistic–continuum model[24] that couples the classical atomistic molecular dynamics (MD) method with the continuum-level two-temperature model (TTM).[25] The model accounts for the laser excitation of conduction-band electrons, electron–phonon coupling, and the fast electron heat conduction from the hot surface region of the irradiated target to the bulk of the target. At the same time, the atomistic representation of the surface region of the target enables detailed analysis of the kinetics and mechanisms of laser-induced structural and phase transformations. A complete description of the combined atomistic-continuum model is provided elsewhere,[5,24] and all the parameters of the model for laser interaction with a Ag target are given in ref 15. Thus, only a brief outline of the computational setup used in the present work is provided below.

The atomistic part of the TTM-MD model represents the top 150 nm surface region of the target and consists of 84.2 million Ag atoms initially arranged into a face-centered cubic (fcc) crystal with (001) surface orientation. The heat transfer in the deeper part of the target is described by the equations of conventional TTM solved down to the depth of 4 μm. This depth is chosen to ensure negligible temperature increase at the bottom of the computational domain during the time of the simulation. At the bottom of the atomistic part of the model, a special pressure-transmitting boundary condition[26,27] is applied in order to avoid an artificial reflection of the laser-induced pressure wave. In the lateral directions, parallel to the (001) surface of the Ag target, the uniform laser energy deposition and periodic boundary conditions are applied, which mimics the conditions in a small region within a laser spot that is much larger than the lateral dimensions of the computational system, 98.7 nm × 98.7 nm.

The interatomic interactions in the atomistic part of the model are described by the embedded atom method (EAM) potential with the functional form and parametrization developed in ref 28. A cutoff function[29] is added to the potential to smoothly bring the interaction energies and forces to zero at interatomic distance of 5.5 Å. While the potential is fitted to low-temperature values of the equilibrium lattice constant, sublimation energy, elastic constants, and vacancy formation energy, it also provides a good description of high-temperature thermodynamic properties of Ag[30] relevant to the simulation of laser-induced processes. The equilibrium melting

DOI: 10.1021/acs.jpcc.6b00013
J. Phys. Chem. C 2016, 120, 4438−4447

temperature predicted with this potential in liquid-crystal coexistence simulations, T_m = 1139 K,[14] is about 8% below the experimental value of 1235 K.[31]

The irradiation of the target with a 100 fs laser pulse at a laser wavelength of 800 nm is represented through a source term added to the equation for the electron temperature.[24] The "ballistic" energy transport occurring before the thermalization of the excited electrons is accounted for by using the effective range of the laser energy deposition, combining the optical absorption depth of 12 nm[32] with the ballistic range of 56 nm estimated for Ag,[15] in place of the optical absorption depth alone in the source term.

3. COMPUTATIONAL RESULTS AND DISCUSSION

3.1. Photomechanical Spallation and Generation of Surface Nanospike. The large-scale TTM-MD simulation discussed in this paper is performed at an absorbed laser fluence of 0.09 J/cm^2, just above the threshold for photomechanical spallation of a liquid layer. A series of snapshots of atomic configurations generated in the simulation are shown in Figure 1, where the atoms are colored according to their local structural environment identified with a method suggested in ref 33 and modified in ref 14, so that the melted regions, crystal phases, and defects generated by the laser irradiation could be clearly identified. The fast melting of ∼80 nm top layer of the irradiated target takes place within the first 100 ps after the laser pulse and is followed by a gradual resolidification of the melted region.

The melting process proceeds simultaneously with the relaxation of the laser-induced stresses, which results in the massive emission of partial and split dislocations from the melting front and triggers the spallation of a top 55 nm thick liquid layer from the bulk of the target. The interactions between dislocations activated in four different {111} slip planes lead to the formation of immobile dislocation segments (so-called stair−rod dislocations) that ensure stability of the dislocation configurations generated during the initial spike of temperature and thermoelastic stresses. The stacking faults left behind by partial dislocations can be seen in Figure 1 as red lines (double atomic layers with local hcp structure) in the parts of the target located below the melting front.

The spallation process, discussed in detail elsewhere,[5,34,35] proceeds through the nucleation, growth, and coalescence of multiple voids in the melted subsurface region of the irradiated target. The evolution of subsurface voids takes place concurrently with the advancement of the solidification front which, at laser fluences just below the spallation threshold, may capture some of the voids and lead to the formation of a subsurface porous region.[15] At a higher fluence used in the present simulation, however, the larger amplitude of the initial compressive stresses generated by the laser energy deposition results in a stronger acceleration of the top liquid layer, whereas the deceleration of the layer due to the work spent on the generation and expansion of the voids is reduced by the higher temperature of the subsurface region. As a result, by the time of ∼800 ps, the growth and coalescence of subsurface voids result in the formation of an elongated liquid bridge that connects the substrate with the top liquid layer. Further extension of the liquid bridge hardly decelerates the top layer that continues to move away from the target at an almost constant velocity of ∼100 m/s. The elongation of the liquid bridge proceeds simultaneously with solidification of a part of the bridge adjacent to the substrate, thus limiting the elongation to the rapidly shrinking liquid part of the bridge. Eventually, at ∼2.9 ns, the liquid part of the bridge breaks down, leading to the formation of a thin frozen nanospike on the surface of the target and the ejection of a 55 nm thick liquid layer. The diameter of nanospike decreases from ∼30 nm at the base down to ∼6 nm at the tip, as can be seen from Figure 2.

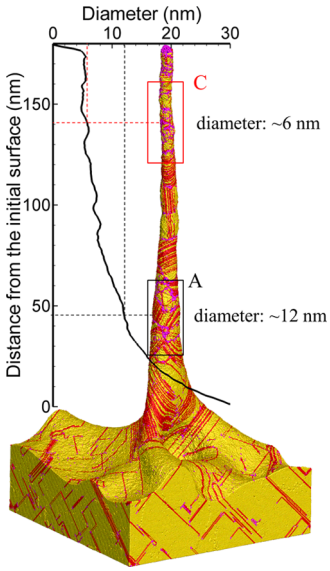

Figure 2. A three-dimensional view of the frozen nanospike generated by the time of 3200 ps in a TTM-MD simulation of laser spallation of a bulk Ag target irradiated by a 100 fs laser pulse at an absorbed fluence of 900 J/m^2. The coloring scale is the same as in Figure 1, and the surface atoms are blanked to expose the underlying structure. The plot shows the variation of the nanospike diameter as a function of the distance from the initial surface. The black and red rectangles marked as A and C outline the regions for which snapshots are shown in Figures 4 and 6, respectively.

The formation of a single frozen nanospike in the simulation indicates that the lateral size of the computational system, ∼100 nm, is comparable to (or smaller than) the characteristic distance between the surface features that can be expected to form in single pulse laser spallation experiments. This observation agrees with the results of experimental imaging of nanoscale surface roughness produced in femtosecond laser processing of metal surfaces,[6−9] although a direct quantitative comparison with the experimental data is hindered by the differences in irradiation conditions (number of laser pulses and relative magnitude of the laser fluence with respect to the spallation threshold) and properties of target materials. These differences may affect not only the characteristic size of the frozen surface features but also their shapes. In the simulation discussed in this paper, the breakdown of the liquid bridge and the separation of the liquid layer occur at a time when a major part of the bridge is already solidified, leading to the prompt completion of the solidification process and formation of a sharp tip of the nanospike (Figures 1 and 2). If the separation of the liquid layer would happen at a time when the whole bridge still remains in the liquid state and the undercooling is not sufficiently high to induce homogeneous solidification, the shape of the bridge could undergo a substantial evolution driven by the minimization of the surface energy. Indeed, the formation of spherical "heads" and bent shapes of the nanospikes are commonly observed in the experimental

DOI: 10.1021/acs.jpcc.6b00013
J. Phys. Chem. C 2016, 120, 4438−4447

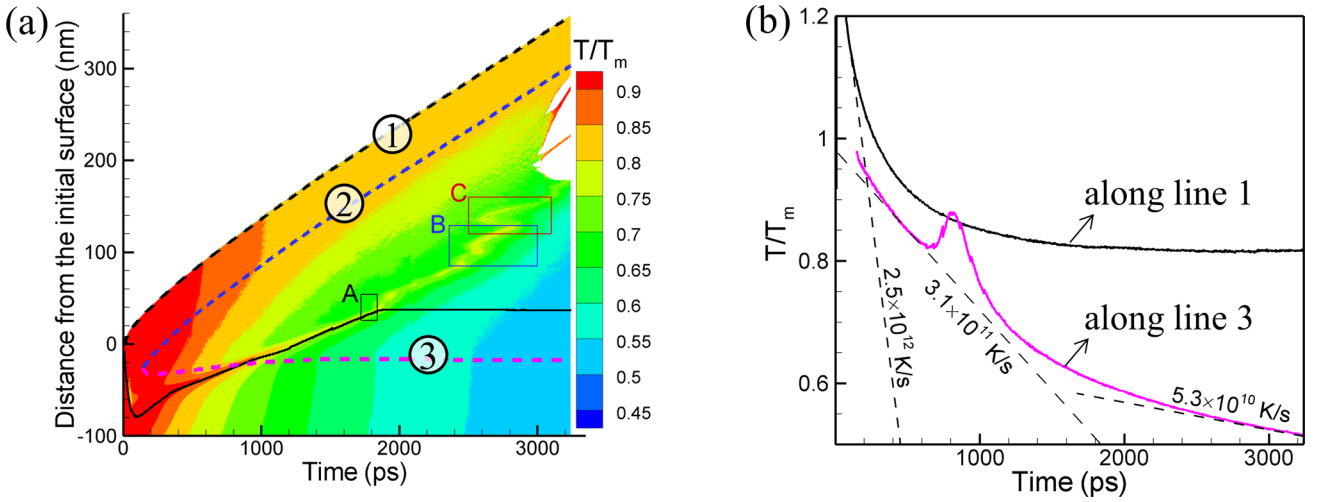

Figure 3. Temperature evolution in the surface region of a bulk Ag target irradiated by a 100 fs laser pulse at an absorbed fluence of 900 J/m^2. In (a), the temperature is shown in the form of a contour plot. The laser pulse directed along the *y*-axis, from the top of the plot. The solid black line shows the location of the melting and solidification fronts, with the latter corresponding to the epitaxial regrowth of the original single-crystal target. The dashed black line, marked 1, follows the position of the outer surface of the target. The dashed blue and purple lines, marked 2 and 3, respectively, outline the inner part of the target where the relative density drops below 50% of the initial density of solid Ag. The black, blue, and red rectangles, marked as A, B, and C, outline the regions and time intervals for which snapshots are shown in Figures 4, 5, and 6, respectively. In (b), the temperature evolution along the dashed black and purple lines 1 and 3 is presented, with several representative cooling rates shown. The temperature is normalized by the equilibrium melting temperature T_m of the EAM Ag.

images.[6,7,9] The random orientations of the heads of the frozen nanospikes generated by single pulse irradiation of a Cu target, revealed in the electron backscatter diffraction measurements,[9] are consistent with the computational prediction of the solidification of the nanospike proceeding through the homogeneous nucleation and growth of new crystallites, discussed in detail in the next two sections.

3.2. Rapid Cooling and Conditions for Homogeneous Crystallization. The dynamics of the spallation process discussed above has a strong effect on the thermal transport and the kinetics of solidification in the surface region of the irradiated target. The temperature evolution in the surface region of the target is shown in Figure 3a in the form of a contour plot. To mark the part of the target where the generation and growth of subsurface voids result in the formation of the elongated bridge, a region where the average density drops below 50% of the initial density of the solid Ag target is outlined by the blue and purple dashed lines (lines 2 and 3 in Figure 3a). The generation of this low-density region hinders the heat flow from the hot surface layer of the target and produces very different long-term temperature profiles in different parts of the target.

The high electronic thermal conductivity of Ag combined with the steep temperature gradients generated by the shallow laser energy deposition result in a very rapid surface cooling, with the maximum cooling rates realized immediately after the electron−phonon equilibration. Indeed, the cooling rate as high as 2.5 × 10^{12} K/s at ∼100 ps after the laser pulse can be deduced from the surface temperature profile shown by the black curve in Figure 3b. With the appearance and expansion of the low-density subsurface region, however, the surface cooling rate quickly decreases as the top liquid layer becomes thermally "insulated" from the substrate. The conductive cooling of the spalled layer comes to the complete end when the liquid bridge breaks down at ∼2.9 ns. In contrast to the surface of the target, the slowdown and eventual interruption of the heat flow from the hot surface layer increase the cooling rate in the part of the target directly underlying the low-density region. The temperature profile shown for this part of the target by the purple curve in Figure 3b indicates that despite the gradual reduction of the cooling rate due to the decreasing temperature gradient, it remains as high as 5.3 × 10^{10} K/s at 3 ns.

The fast cooling of the deeper regions of the target brings the temperature of the liquid−solid interface to the levels below the equilibrium melting temperature by the time of ∼100 ps and activates resolidification that proceeds through the epitaxial regrowth of the substrate. The solidification front propagates toward the surface of the target at a velocity of ∼60 m/s as can be seen from the snapshots in Figure 1 and the shape of the solid black line marking the position of solidification front in Figure 3a. At ∼800 ps the solidification front reaches the base of the elongated liquid bridge, causing the local spike in the temperature profile shown by the purple curve of Figure 3b. The temperature spike at the solidification front is related to the release of the latent heat of solidification and can also be observed in the temperature contour plot shown in Figure 3a.

By the time the solidification front reaches the low-density region, all but one of the voids have already coalesced to produce a single liquid bridge connecting the target with the top liquid layer. The remaining void is located at the very base of the liquid bridge and is stabilized by the tensile stresses supported by the continuous elongation of the bridge. During the time between 800 ps and 1.2 ns, the solidification front advances in the regions immediately adjacent to the void and fully embeds it into the crystalline surroundings, as can be seen from the snapshots shown in Figure 1.

Further propagation of the solidification front proceeds simultaneously with the increase in the level of undercooling of the lower part of the liquid bridge. When the temperature of the liquid part of the bridge drops below a certain level, found in ref 15 to be ∼0.69 T_m for the EAM Ag, an onset of active homogeneous nucleation of new crystallites in the deeply undercooled liquid can be expected and, indeed, is observed staring from the time of ∼1720 ps. The microscopic

DOI: 10.1021/acs.jpcc.6b00013
J. Phys. Chem. C 2016, 120, 4438−4447

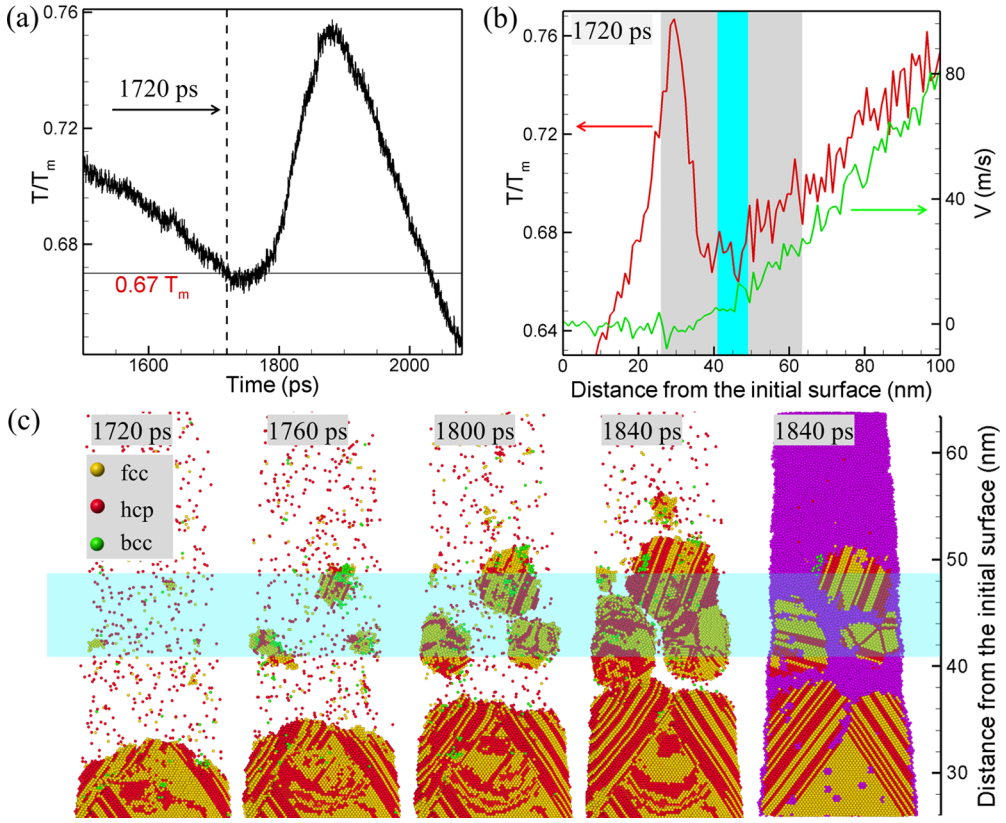

Figure 4. Temperature profiles and snapshots illustrating the conditions and mechanisms of homogeneous nucleation and growth of crystallites in a region marked by rectangle A in Figures 1, 2, and 3. In (a), the temperature evolution is shown for a region where homogeneous nucleation of new crystallites is observed, between 41 and 49 nm above the initial surface of the target. This region is marked by the light blue stripe in (b) and (c). In (b), the temperature and material flow velocity profiles are shown for a time of 1720 ps, when the homogeneous nucleation is first observed. In (c), the snapshots illustrating the homogeneous nucleation and growth are provided for a region marked by gray color in (b). The atoms are colored by their local structural environments as in Figure 1, with green color used for bcc atoms. The purple atoms (liquid phase, surfaces, and defects) are blanked in the first four snapshots to provide clear views of the nucleation and growth of new grains, while a cross section similar to the ones in Figure 1 is shown in the last snapshot.

mechanisms of the homogeneous nucleation and growth of new crystallites are discussed in section 3.3, while here we provide additional comments on the role of the spallation process in creating the conditions of deep undercooling required for the onset of homogeneous crystallization.

It turns out that the generation of voids and the formation of the liquid bridge play the key roles in achieving the sufficiently high levels of undercooling. In particular, the process of the bridge elongation takes more than 2 ns and proceeds with an elongation velocity, ∼100 m/s, which is higher than the velocity of the solidification front propagation, ∼60 m/s. While the heat flow from the hot surface layer continues to keep the upper part of the bridge at a temperature slightly above $0.8T_m$, the temperature right above the solidification front decreases and drops below $0.7T_m$ by 1.6 ns, as can be seen from the corresponding temperature profiles shown in Figure 1. The breakdown of the bridge at ∼2.9 ns interrupts the connection to the top layer that has been serving as a "heat reservoir" supporting the quasi-steady-state heat flow in the bridge. As a result, the rapid electron heat conduction to the bulk of the target leads to an almost immediate flattening of the electron temperature profile, as can be seen from the plots shown next to the last snapshot in Figure 1. The cooling of the tip of the bridge in this case is very rapid and is only limited by the strength of the electron−phonon coupling. In fact, the idea of achieving fast cooling by linking a hot thin bridge with a cold substrate has recently been exploited for achieving an extreme cooling rate of 10^{14} K/s leading to the formation of a monatomic metallic glass.[36]

Note that in the absence of the void nucleation and spallation, the complete resolidification of the target would take ∼1.4 ns and the maximum undercooling realized by the time the solidification front reaches the surface does not exceed 25%, as estimated in a TTM calculation accounting for the temperature dependence of the solidification front velocity.[3] On the other hand, if we assume that the spallation happens instantaneously, without the formation of an intermediate low density region and liquid bridges, the complete epitaxial regrowth of the remaining part of the target would only take 930 ps and the maximum undercooling of the melted surface would be ∼22%. We can conclude, therefore, that the generation of subsurface voids and liquid bridges in the course of the spallation process is essential for creating the conditions of undercooling that is sufficiently strong for the activation of rapid homogeneous crystallization. This conclusion is supported by the results of a simulation performed at a lower laser fluence, below the spallation threshold,[15] where the slowdown of the motion of epitaxial solidification front in a region affected by the evolution of subsurface voids is found to extend the time of the solidification and create the conditions for nanocrystallization of a surface layer.

DOI: 10.1021/acs.jpcc.6b00013
J. Phys. Chem. C 2016, 120, 4438−4447

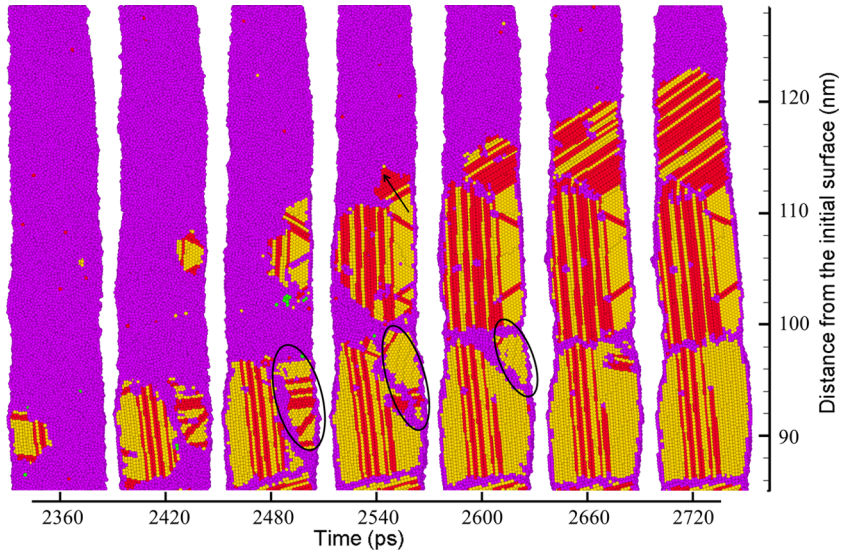

Figure 5. Snapshots providing an enlarged view of the region marked by rectangle B in Figures 1 and 3. Similar to Figure 1, the cross sections of the nanospike are shown in the snapshots. The atoms are colored by their local structural environment, as explained in captions for Figures 1 and 4. The snapshots illustrate the nucleation and growth of crystallites with mixed fcc/hcp structure, coarsening of the grains (disappearance of a small grain outlined by ovals in three snapshots), and cross-nucleation of hcp platelets on {111} faces of growing fcc crystallites (an example is marked by the black arrow in a snapshot shown for 2540 ps).

3.3. Microscopic Mechanisms of Homogeneous Nucleation and Growth. As discussed in the previous section, the propagation of the solidification front takes place under conditions of increasing undercooling of the remaining liquid metal. By the time of 1720 ps, the temperature of the liquid in the immediate vicinity of the solidification front drops down to ~0.67 T_m (Figures 4a and 4b) and triggers rapid homogeneous nucleation of new crystallites (Figure 4c). Three crystal nuclei with random crystallographic orientations appear almost simultaneously at 1720 ps in the deeply undercooled liquid region, grow, and merge with the front of the epitaxial solidification by ~1840 ps. The onset of the homogeneous crystallization locks the interface between the single crystal part of the target solidified through the epitaxial regrowth of the substrate and the nanocrystalline region generated by the homogeneous nucleation and growth of new crystallites at the position of ~37.5 nm above the initial surface target, as reflected by flattening of the solid black line in Figure 3a after 1840 ps.

Similar to the epitaxial regrowth, the rapid release of the latent heat of solidification due to the homogeneous nucleation and growth of new crystallites leads to a pronounced increase in the local temperature, as can be seen in Figure 4a. The nucleation and growth of multiple crystallites can be clearly identified by the scattered temperature spikes in the contour plot shown in Figure 3a and is reflected in broadening of the temperature peaks in the profiles shown for 2.4 and 2.8 ns in Figure 1. Note that despite the high lattice temperature gradients produced in the immediate vicinity of regions undergoing either heterogeneous or homogeneous solidification, the heating of the surrounding areas is limited due to the essentially flat electron temperature profiles, as can be seen in Figure 1. The cooling of the regions heated by the release of the latent heat of solidification is largely defined by the local electron−phonon equilibration rather than the vibrational/phononic heat transport. Similar splitting of the electron and lattice temperatures has been reported in earlier TTM and TTM-MD simulations of rapid nonequilibrium melting[37] and solidification.[3,13]

The highly nonequilibrium nature of the rapid solidification process, when the nucleation and growth of new crystallites take place under conditions of deep undercooling, along with the low stacking-fault energy of Ag,[38] result in the formation of a high density of the stacking faults, twins, and the mixed fcc−hcp structures. With this coloring scheme used in the snapshots shown in the figures, single and double red atomic planes on yellow background correspond to twin boundaries and stacking faults in the fcc structure, respectively, while thicker red platelets are the regions with hcp structure. The fcc and hcp regions in the nanograins have $\langle 111\rangle_{fcc}//\langle 0001\rangle_{hcp}$ orientation relationship and form through cross-nucleation of the metastable hcp phase on structurally compatible {111} faces of growing fcc crystallites, as exemplified by the growth of a grain marked by the black arrow in a snapshot shown for 2540 ps in Figure 5.

A similar process of cross-nucleation of the hcp phase on {111} faces of fcc nuclei has been observed in atomistic simulations of liquid Cu undercooled to 0.69T_m[39] as well as in undercooled Lennard-Jones liquids.[40,41] The high probability of nucleation of an atomic layer with hcp stacking sequence on a {111} facet of the growing fcc crystal is related to the relatively low energies of coherent twin boundaries and stacking faults as compared to the strong driving force for the solidification. The generation of a sequence of close-packed planes that corresponds to a stacking fault can serve as a nucleus for the subsequent growth of the metastable hcp structure. The coexistence of fcc and hcp grains has also been observed in pulsed laser deposited nanocrystalline Ni films,[42] where the formation of stacking faults on in-plane {111} faces of growing fcc grains is considered to be the mechanism leading to the cross-nucleation of hcp grains.

Even though the growing crystallites have predominantly fcc/hcp structure, the structural analysis also reveals the presence of small bcc crystallites that transiently appear around the growing close-packed crystallites grains (green clusters in

DOI: 10.1021/acs.jpcc.6b00013
J. Phys. Chem. C 2016, 120, 4438−4447

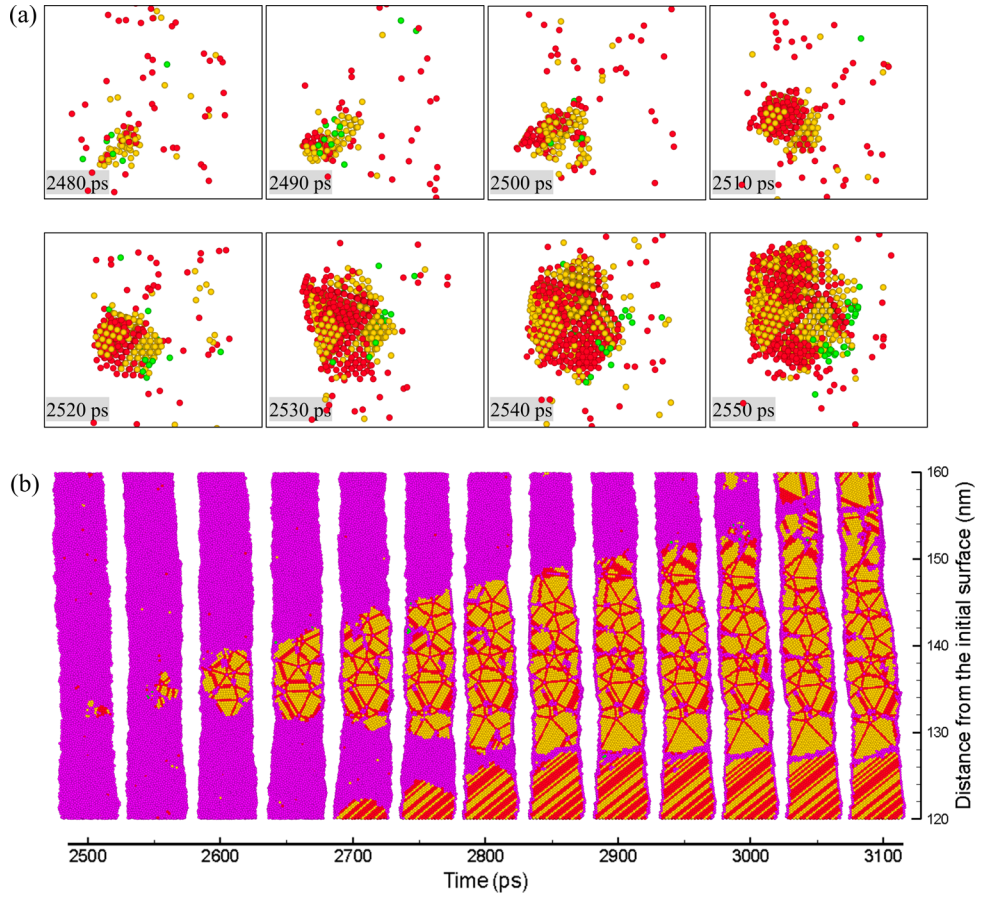

Figure 6. Snapshots illustrating the nucleation of the first pentagonal twinned structure (a) and the subsequent growth of a nanostructure featuring multiple axis of 5-fold symmetry (b) in the region marked by rectangle C in Figures 1, 2, and 3. The atoms are colored by their local structural environment, as explained in captions for Figures 1 and 4. In (a), the atoms that belong to the liquid phase, crystal defects, and the free surface of the target are blanked to provide an unobstructed view of the nucleation process. In (b), the cross sections of the nanospike are shown.

Figures 4c, 5, and 6). This observation can be related to the results of atomistic simulations of crystal nucleation in Lennard-Jones systems undercooled down to $0.75-0.8T_m$,[40,43,44] where transient appearance of small bcc clusters "wetting" the surface of the growing fcc crystallites is observed.

After the growing grains join together and form nanocrystalline structure of the nanospike, some additional structural rearrangements driven by the minimization of energy of the internal structure of the grains, as well as their interfacial and surface energy, take place. The internal structure is changing largely through the glide of partial dislocations across close-packed atomic planes, which alters the stacking sequence of planes between the fcc and hcp types. The grain coarsening also takes place, as illustrated by the disappearance of a small grain outlined by ovals in Figure 5. The coarsening results in the formation of two elongated grains extending through the whole thickness of the nanospike and occupying the lower part of the region shown in Figure 5. In each grain, one of the ⟨110⟩ crystallographic directions is roughly aligned with the axis of the nanospike, which allows for the local surface energy minimization in the corresponding parts of the nanospike.[45]

3.4. Generation of a Region with Icosahedral Structure. As the solidification process moves up along the nanospike, we observe the formation of an extended region of the nanospike that features a markedly distinct nanostructure. In contrast with the single orientation of twin boundaries, stacking faults, and hcp platelets in the grains discussed in section 3.3 and illustrated in Figure 5, the solidification of a region located between 130 and 150 nm above the initial surface of the target and outlined by rectangle C in Figures 1, 2, and 3a produces a continuous network of pentagonal twinned structural elements (Figure 6b). Similarly to the lower parts of the nanospike, the solidification of this region proceeds through the homogeneous nucleation and growth of the solid structures, as can be seen from Figure 6a. Moreover, the conditions of the homogeneous nucleation are also very similar to the ones discussed above and illustrated in Figure 4. The maximum level of undercooling reached in the nucleation region, between 128 and 138 nm, by the time of the appearance of a stable solid nucleus, 2480 ps, is about 30%, which is similar to the 33% undercooling at the time of the nucleation of new grains in the lower part of the nanospike (Figure 4a). Thus, the formation of the distinct pentagonal twinned structure of the upper region of the nanospike cannot be attributed to the difference in the levels of undercooling at the time of the nucleation and growth but is likely to be selected in the course of the nucleation and then replicated during the growth process. This hypothesis can be supported by detailed analysis of snapshots taken every 10 ps during the nucleation process and shown in Figure 6a.

The first stable crystallite can be identified in this region of the nanospike at 2480 ps. The crystallite has largely fcc structure, but a small island of a close-packed plane with local hcp stacking sequence can be identified on one of the four {111} faces of the growing fcc crystallite as earlier as 2490 ps.

DOI: 10.1021/acs.jpcc.6b00013
J. Phys. Chem. C 2016, 120, 4438−4447

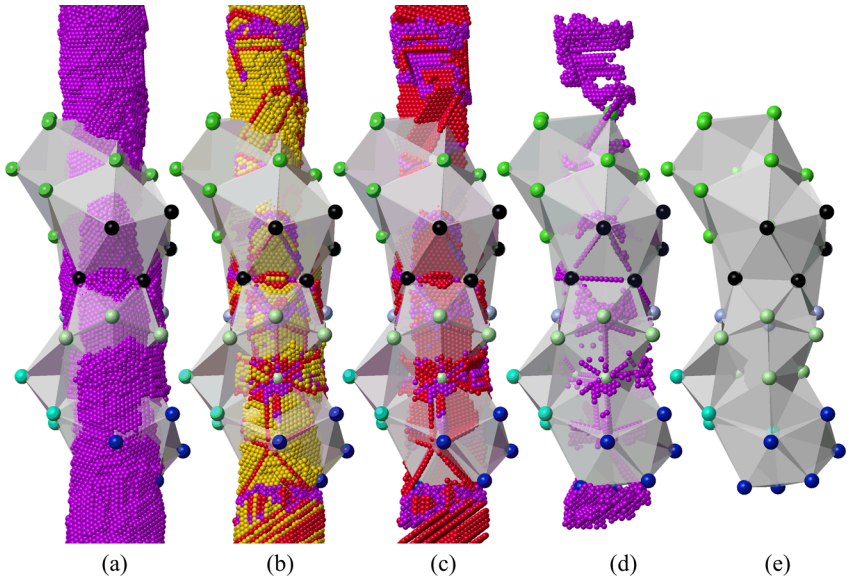

Figure 7. Result of the structural analysis of a part of the frozen nanospike located between 125 and 155 nm above the initial surface of the irradiated target. The structure of this region can be represented by six interpenetrating icosahedra truncated by the free surface of the nanospike. The atoms are colored by their local structural environment, as explained in captions for Figures 1 and 4. All atoms are shown in (a), surface atoms are blanked in (b), both surface and fcc atoms are blanked in (c), surface, fcc, and hcp atoms are blanked in (d), and all atoms are blanked in (e), where only the six interpenetrating icosahedra are shown.

Further growth of the crystallite turns the hcp layer into a twin boundary that separates two fcc crystallites misoriented with respect to each other so that the only common {111} plane they share is the plane of the twin boundary. A similar process leads to the formation of another hcp plane/twin boundary on a different face of the original crystallite. The two twin boundaries intersect each other along a common ⟨110⟩ direction in the fcc crystallites, and the intersection serves as a catalyst for the formation of decahedral local atomic structure and nucleation of three additional twin boundaries upon further growth of the solid region.[41] This growth scenario results in the formation of a decahedral twined structure composed of five tetrahedral fcc domains separated from each other by twin boundaries and joined together along a common axis of 5-fold symmetry, as can be seen in the last snapshot in Figure 6a.

Further growth of the twinned structure proceeds through similar fcc−twin−fcc cycle repeated for different {111} faces of the growing tetrahedral fcc domains. Indeed, the appearance of a close-packed plane with hcp stacking on any of the ten {111} faces of the decahedral structure generates two more twin boundary intersections, which result in the formation of two new pentagonal axis of symmetry in the growing nanostructured region. This process of repetitive growth twinning and generation of new tetrahedral fcc domains arranged around 5-fold axes results in the formation of a complex continuous network composed of pentagonal twinned structural elements in a more than 20 nm long region of the nanospike (Figure 6b). A detailed structural analysis reveals that the structure of this region of the nanospike can be represented by an assembly of tetrahedral fcc domains arranged into six interpenetrating icosahedra truncated by the free surface of the nanospike, as illustrated in Figure 7.

The formation of the nanostructure featuring multiple axis of 5-fold symmetry is possible due to the fact that the angle between two close-packed {111} planes in the fcc lattice is 70.53°, and 70.53° × 5 = 352.65° is only 7.35° short of 360°. As a result, the arrangement of five perfect tetrahedral fcc domains into a compact decahedral structure leaves a 7.35° solid angle gap. Closing this gap by rotational deformation of the decahedral structure is equivalent to the introduction of a positive wedge disclination[46,47] with strength (Frank vector) equal to 7.35° along the pentagonal axis of the decahedron. Similarly, an icosahedral arrangement of 20 tetrahedral domains corresponds to the introduction of six disclinations passing through all the pentagonal axes of the icosahedron. While the interfacial/surface energy of the decahedral and icosahedral structures is minimized by the presence of {111} crystallographic facets only, the strong quadratic dependence of the elastic strain energy of a disclination on the size of the crystal precludes the formation of large-scale twinned decahedral and icosahedral structures. In the case of the nanospike, however, the elastic strain energy of the disclinations is reduced by the small size of the pentagonal structural elements and the presence of the free surface of the nanospike. The size effect has also been observed in simulations of freezing of Au nanoclusters,[48] where the probability of the formation of icosahedral structure of a frozen cluster was observed to increase when the nanocluster diameter decreases from 5 to 2 nm. At the qualitative level, the generation of the polyicosahedral structure in the thinnest part of the nanospike with diameter of ∼6 nm and the formation of mixed fcc/hcp structure in the thicker lower parts with diameter of ∼12 nm (Figure 2) are consistent with this general trend.

To summarize, the formation of an extended region of polyicosahedral structure can be attributed to the smaller diameter of the nanospike and the stochastic selection made at the initial stage of the homogeneous solidification process. The formation and intersection of two close-packed atomic layers with hcp stacking on {111} planes of a tetrahedral fcc crystallite trigger a self-replicating process of generation of multiple axes of pentagonal symmetry arranged into a continuous network outlining the fcc tetrahedral structural units of the polyicosahedral structure. The stochastic selection between the layered fcc/hcp crystallites and twinned tetrahedral structures featuring 5-

DOI: 10.1021/acs.jpcc.6b00013
J. Phys. Chem. C 2016, 120, 4438−4447

fold axes of symmetry have been observed in simulations of vapor-phase growth[49] and freezing[50,51] of nanoparticles as well as in solidification of strongly undercooled bulk (periodic boundary conditions) liquids.[39,41] In the present simulation, we observe a direct competition of the two solidification scenarios that are realized simultaneously in different parts of the strongly undercooled liquid bridge and produce solid regions with two distinct nanocrystalline structures shown in Figures 5 and 6.

4. SUMMARY

The results of a large-scale atomistic simulation of laser interaction with a Ag target irradiated by a femtosecond laser pulse provide detailed information on the mechanisms responsible for the formation of a frozen nanospike on the irradiated surface as well as on the processes that define the complex nanostructure of the nanospike. The simulation is performed in the spallation irradiation regime, when the relaxation of laser-induced stresses induces nucleation, growth, and coalescence of multiple voids in the melted subsurface region of the irradiated target. The evolution of the subsurface voids results in the formation and eventual breakdown of an elongated liquid bridge that solidifies and produces a ~200 nm long frozen nanospike.

The spallation process is also responsible for creating conditions of a deep undercooling (down to $0.7T_m$ and more) in the upper part of the liquid bridge, which sets the stage for the competition between the epitaxial regrowth of the solid part of the target and the homogeneous nucleation of new crystallites. The homogeneous solidification proceeds along two distinct paths selected at the crystal nucleation stage and produces markedly different nanostructures in different parts of the nanospike. The growth proceeding through the cross-nucleation of hcp and fcc regions on close-packed faces of the growing crystallites produces grains with mixed fcc/hcp structure and one dominant orientation of twin boundaries, stacking faults, and hcp/fcc interfaces. The nucleation process that involves the formation of a pair of close-packed atomic layers with hcp stacking on adjacent {111} faces of a small fcc crystallite, on the other hand, steers the subsequent growth in the direction of self-replicating generation of multiple axes of pentagonal symmetry arranged into a polyicosahedral structure. Overall, the competing contributions of several solidification mechanisms activated under highly nonequilibrium solidification conditions result in a remarkable variability of the structural motifs in the frozen surface nanospike generated by laser spallation of a Ag target.

AUTHOR INFORMATION

Corresponding Author

*E-mail: lz2n@virginia.edu (L.V.Z.).

Notes

The authors declare no competing financial interest.

ACKNOWLEDGMENTS

Financial support for this work was provided by the National Science Foundation (NSF) through Grant CMMI-1301298 and the Air Force Office of Scientific Research through Grant FA9550-10-1-0541. Computational support was provided by the Oak Ridge Leadership Computing Facility (Project MAT048) and NSF through the Extreme Science and Engineering Discovery Environment (Project TG-DMR110090). The authors thank Maxim Shugaev for his help with TTM calculations of laser-induced surface melting and resolidification.

REFERENCES

(1) Lin, C.-J.; Spaepen, F.; Turnbull, D. Picosecond pulsed laser-induced melting and glass formation in metals. *J. Non-Cryst. Solids* **1984**, *61*−*62*, 767−772.
(2) Duff, W. H.; Zhigilei, L. V. Computational study of cooling rates and recrystallization kinetics in short pulse laser quenching of metal targets. *J. Phys.: Conf. Ser.* **2007**, *59*, 413−417.
(3) Chan, W.-L.; Averback, R. S.; Cahill, D. G.; Ashkenazy, Y. Solidification velocities in deeply undercooled silver. *Phys. Rev. Lett.* **2009**, *102*, 095701.
(4) Ivanov, D. S.; Lin, Z.; Rethfeld, B.; O'Connor, G. M.; Glynn, Th. J.; Zhigilei, L. V. Nanocrystalline structure of nanobump generated by localized photo-excitation of metal film. *J. Appl. Phys.* **2010**, *107*, 013519.
(5) Wu, C.; Zhigilei, L. V. Microscopic mechanisms of laser spallation and ablation of metal targets from large-scale molecular dynamics simulations. *Appl. Phys. A: Mater. Sci. Process.* **2014**, *114*, 11−32.
(6) Vorobyev, A. Y.; Guo, C. Enhanced absorptance of gold following multipulse femtosecond laser ablation. *Phys. Rev. B: Condens. Matter Mater. Phys.* **2005**, *72*, 195422.
(7) Zhao, Q.-Z.; Malzer, S.; Wang, L.-J. Self-organized tungsten nanospikes grown on subwavelength ripples induced by femtosecond laser pulses. *Opt. Express* **2007**, *15*, 15741−15746.
(8) Dai, Y.; He, M.; Bian, H.; Lu, B.; Yan, X.; Ma, G. Femtosecond laser nanostructuring of silver film. *Appl. Phys. A: Mater. Sci. Process.* **2012**, *106*, 567−574.
(9) Oboňa, J. V.; Ocelík, V.; Rao, J. C.; Skolski, J. Z. P.; Römer, G. R. B. E.; Huis in 't Veld, A. J.; De Hosson, J. Th. M. Modification of Cu surface with picosecond laser pulses. *Appl. Surf. Sci.* **2014**, *303*, 118−124.
(10) MacDonald, C. A.; Malvezzi, A. M.; Spaepen, F. Picosecond time-resolved measurements of crystallization in noble metals. *J. Appl. Phys.* **1989**, *65*, 129−136.
(11) Agranat, M. B.; Ashitkov, S. I.; Fortov, V. E.; Kirillin, A. V.; Kostanovskii, A. V.; Anisimov, S. I.; Kondratenko, P. S. Use of optical anisotropy for study of ultrafast phase transformations at solid surfaces. *Appl. Phys. A: Mater. Sci. Process.* **1999**, *69*, 637−640.
(12) Chen, J.; Chen, W.-K.; Tang, J.; Rentzepis, P. M. Time-resolved structural dynamics of thin metal films heated with femtosecond optical pulses. *Proc. Natl. Acad. Sci. U. S. A.* **2011**, *108*, 18887−18892.
(13) Lin, Z.; Johnson, R. A.; Zhigilei, L. V. Computational study of the generation of crystal defects in a bcc metal target irradiated by short laser pulses. *Phys. Rev. B: Condens. Matter Mater. Phys.* **2008**, *77*, 214108.
(14) Wu, C.; Thomas, D. A.; Lin, Z.; Zhigilei, L. V. Runaway lattice-mismatched interface in an atomistic simulation of femtosecond laser irradiation of Ag film - Cu substrate system. *Appl. Phys. A: Mater. Sci. Process.* **2011**, *104*, 781−792.
(15) Wu, C.; Christensen, M. S.; Savolainen, J.-M.; Balling, P.; Zhigilei, L. V. Generation of sub-surface voids and a nanocrystalline surface layer in femtosecond laser irradiation of a single crystal Ag target. *Phys. Rev. B: Condens. Matter Mater. Phys.* **2015**, *91*, 035413.
(16) Zhao, S.; Hahn, E. N.; Kad, B.; Remington, B. A.; Wehrenberg, C. E.; Bringa, E. M.; Meyers, M. A. Amorphization and nanocrystallization of silicon under shock compression. *Acta Mater.* **2016**, *103*, 519−533.
(17) Weck, A.; Crawford, T. H. R.; Borowiec, A.; Wilkinson, D. S.; Preston, J. S. Femtosecond laser-based fabrication of a new model material to study fracture. *Appl. Phys. A: Mater. Sci. Process.* **2007**, *86*, 55−61.
(18) Kumar, A.; Pollock, T. M. Mapping of femtosecond laser-induced collateral damage by electron backscatter diffraction. *J. Appl. Phys.* **2011**, *110*, 083114.
(19) Sedao, X.; Maurice, C.; Garrelie, F.; Colombier, J.-P.; Reynaud, S.; Quey, R.; Blanc, G.; Pigeon, F. Electron backscatter diffraction

DOI: 10.1021/acs.jpcc.6b00013
J. Phys. Chem. C 2016, 120, 4438−4447

characterization of laser-induced periodic surface structures on nickel surface. *Appl. Surf. Sci.* **2014**, *302*, 114−117.
(20) Sedao, X.; Maurice, C.; Garrelie, F.; Colombier, J.-P.; Reynaud, S.; Quey, R.; Pigeon, F. Influence of crystal orientation on the formation of femtosecond laser-induced periodic surface structures and lattice defects accumulation. *Appl. Phys. Lett.* **2014**, *104*, 171605.
(21) Savolainen, J.-M.; Christensen, M. S.; Balling, P. Material swelling as the first step in the ablation of metals by ultrashort laser pulses. *Phys. Rev. B: Condens. Matter Mater. Phys.* **2011**, *84*, 193410.
(22) Ionin, A. A.; Kudryashov, S. I.; Ligachev, A. E.; Makarov, S. V.; Seleznev, L. V.; Sinitsyn, D. V. Nanoscale cavitation instability of the surface melt along the grooves of one-dimensional nanorelief gratings on an aluminum surface. *JETP Lett.* **2011**, *94*, 266−269.
(23) Ashitkov, S. I.; Inogamov, N. A.; Zhakhovskii, V. V.; Emirov, Yu. N.; Agranat, M. B.; Oleinik, I. I.; Anisimov, S. I.; Fortov, V. E. Formation of nanocavities in the surface layer of an aluminum target irradiated by a femtosecond laser pulse. *JETP Lett.* **2012**, *95*, 176−181.
(24) Ivanov, D. S.; Zhigilei, L. V. Combined atomistic-continuum modeling of short pulse laser melting and disintegration of metal films. *Phys. Rev. B: Condens. Matter Mater. Phys.* **2003**, *68*, 064114.
(25) Anisimov, S. I.; Kapeliovich, B. L.; Perel'man, T. L. Electron emission from metal surfaces exposed to ultrashort laser pulses. *Sov. Phys. JETP* **1974**, *39*, 375−377.
(26) Zhigilei, L. V.; Garrison, B. J. Pressure waves in microscopic simulations of laser ablation. *Mater. Res. Soc. Symp. Proc.* **1999**, *538*, 491−496.
(27) Schafer, C.; Urbassek, H. M.; Zhigilei, L. V.; Garrison, B. J. Pressure-transmitting boundary conditions for molecular dynamics simulations. *Comput. Mater. Sci.* **2002**, *24*, 421−429.
(28) Foiles, S. M.; Baskes, M. I.; Daw, M. S. Embedded-atom-method functions for the fcc metals Cu, Ag, Au, Ni, Pd, Pt, and their alloys. *Phys. Rev. B: Condens. Matter Mater. Phys.* **1986**, *33*, 7983−7991.
(29) Voter, A. F.; Chen, S. P. Accurate interatomic potentials for Ni, Al, and Ni_3Al. *Mater. Res. Soc. Symp. Proc.* **1999**, *82*, 175−180.
(30) Foiles, S. M.; Adams, J. B. Thermodynamic properties of fcc transition metals as calculated with embedded-atom method. *Phys. Rev. B: Condens. Matter Mater. Phys.* **1989**, *40*, 5909−5915.
(31) Weast, R. C. *Handbook of Chemistry and Physics*, 64th ed.; CRC Press: Boca Raton, FL, 1983.
(32) Bäuerle, D. *Laser Processing and Chemistry*; Springer-Verlag: Berlin, 2000.
(33) Ackland, G. J.; Jones, A. P. Applications of local crystal structure measures in experiment and simulation. *Phys. Rev. B: Condens. Matter Mater. Phys.* **2006**, *73*, 054104.
(34) Leveugle, E.; Ivanov, D. S.; Zhigilei, L. V. Photomechanical spallation of molecular and metal targets: molecular dynamics study. *Appl. Phys. A: Mater. Sci. Process.* **2004**, *79*, 1643−1655.
(35) Zhigilei, L. V.; Garrison, B. J. Microscopic mechanisms of laser ablation of organic solids in the thermal and stress confinement irradiation regimes. *J. Appl. Phys.* **2000**, *88*, 1281−1298.
(36) Zhong, L.; Wang, J.; Sheng, H.; Zhang, Z.; Mao, S. X. Formation of monatomic metallic glasses through ultrafast liquid quenching. *Nature* **2014**, *512*, 177−180.
(37) Ivanov, D. S.; Zhigilei, L. V. Kinetic limit of heterogeneous melting in metals. *Phys. Rev. Lett.* **2007**, *98*, 195701.
(38) Deng, C.; Sansoz, F. Fundamental differences in the plasticity of periodically twinned nanowires in Au, Ag, Al, Cu, Pb and Ni. *Acta Mater.* **2009**, *57*, 6090−6101.
(39) E, J. C.; Wang, L.; Cai, Y.; Wu, H. A.; Luo, S. N. Crystallization in supercooled liquid Cu: Homogeneous nucleation and growth. *J. Chem. Phys.* **2015**, *142*, 064704.
(40) Desgranges, C.; Delhommelle, J. Molecular mechanism for the cross-nucleation between polymorphs. *J. Am. Chem. Soc.* **2006**, *128*, 10368−10369.
(41) Zhang, H.-J.; Peng, S.-M.; Zhou, X.-S.; Ju, X. Polymorphic crystals selected in the nucleation stage. *Europhys. Lett.* **2014**, *107*, 46002.
(42) Rajasekhara, S.; Ganesh; Hattar, K. J.; Knapp, J. A.; Ferreira, P. J. Evidence of metastable hcp phase grains in as-deposited nanocrystalline nickel films. *Scr. Mater.* **2012**, *67*, 189−192.
(43) ten Wolde, P. R.; Ruiz-Montero, M. J.; Frenkel, D. Numerical evidence for bcc ordering at the surface of a critical fcc nucleus. *Phys. Rev. Lett.* **1995**, *75*, 2714−2717.
(44) Moroni, D.; ten Wolde, P. R.; Bolhuis, P. G. Interplay between structure and size in a critical crystal nucleus. *Phys. Rev. Lett.* **2005**, *94*, 235703.
(45) Maurer, F.; Brötz, J.; Karim, S.; Tomil-Molares, M. E.; Trautmann, C.; Fuess, H. Preferred growth orientation of metallic fcc nanowires under direct and alternating electrodeposition conditions. *Nanotechnology* **2007**, *18*, 135709.
(46) Gryaznov, V. G.; Heydenreich, J.; Kaprelov, A. M.; Nepijko, S. A.; Romanov, A. E.; Urban, J. Pentagonal symmetry and disclinations in small particles. *Cryst. Res. Technol.* **1999**, *34*, 1091−1119.
(47) Romanov, A. E.; Kolesnikova, A. L. Application of disclination concept to solid structures. *Prog. Mater. Sci.* **2009**, *54*, 740−769.
(48) Chushak, Y. G.; Bartell, L. S. Melting and freezing of gold nanoclusters. *J. Phys. Chem. B* **2001**, *105*, 11605−11614.
(49) Polak, W. Formation of regular polyicosahedral and defected crystalline structures in growing Lennard-Jones clusters. *J. Cryst. Growth* **2014**, *401*, 44−50.
(50) Rossi, G.; Ferrando, R. Freezing of gold nanoclusters into polydecahedral structures. *Nanotechnology* **2007**, *18*, 225706.
(51) Asuquo, C. C.; Bowles, R. K. Molecular dynamics simulations of competitive freezing in gold nanoclusters. *J. Phys. Chem. C* **2012**, *116*, 14619−14626.

DOI: 10.1021/acs.jpcc.6b00013
J. Phys. Chem. C 2016, 120, 4438−4447